Independent Component Analysis Tractography Combined with a Ball–Stick Model to Isolate Intravoxel Crossing Fibers of the Corticospinal Tracts in Clinical Diffusion MRI

Jeong-Won Jeong,[1–3]* Eishi Asano,[1,2] Fang-Cheng Yeh,[4] Diane C. Chugani,[1–3,5] and Harry T. Chugani[1–3,5]

The independent component analysis (ICA) tractography method has improved the ability to isolate intravoxel crossing fibers; however, the accuracy of ICA is limited in cases with voxels in local clusters lacking sufficient numbers of fibers with the same orientations. To overcome this limitation, the ICA was combined with a ball–stick model (BSM) ["ICA+BSM"]. An ICA approach is applied to identify crossing fiber components in voxels of small cluster, which are maximally independent in orientation. The eigenvectors of these components are numerically optimized via the subsequent BSM procedure. Simulation studies for two or three crossing fibers demonstrate that ICA+BSM overcomes the limitation of the original ICA method by refining regional ICA solutions in diffusion measurement of a single voxel. It shows 2°–5° of angular errors to isolate two or three fibers, providing a better recovery of simulated fibers compared with ICA alone. Human studies show that ICA+BSM achieves high anatomical correspondence of corticospinal tracts compared with postmortem corticospinal histology, yielding 92.2% true positive detection including both lateral and medial projections, compared with 84.1% for ICA alone. This study demonstrates that the intravoxel crossing fiber problem in clinical diffusion MRI may be sorted out more efficiently by combining ICA with BSM. **Magn Reson Med 70:441–453, 2013.** ©**2012 Wiley Periodicals, Inc.**

Key words: independent component analysis; ball–stick model; lateral projection of corticospinal tract; diffusion-weighted MRI; tractography

A common problem encountered in the streamline tractography of white matter fiber systems when relying on a rank-2 diffusion tensor model (1,2) is the existence of multiple fiber orientations within an imaging voxel. The simple diffusion tensor model used routinely in streamline tractography is inadequate in modeling the probability density function of water displacement when the model is affected by complex fiber arrangement (3). In such a situation, the primary eigenvector of a rank-2 tensor model of a voxel's diffusion field is likely to point in an erroneous direction, biased toward the highest density fibers thus designating many tracts to seemingly propagate in the wrong direction (4). This intravoxel problem limits current diffusion-weighted imaging (DWI) technology in clinical applications.

The strategies to solve the intravoxel problem have included various methods relying on a more complex model characterizing diffusion signals acquired by high angular resolution diffusion imaging, which samples data on a shell in the diffusion encoding q-space (5). The candidate methods include the Gaussian mixture model such as the ball–stick model (BSM) (5–8), the generalized diffusion tensor (9,10), spherical harmonic decomposition (11), and spherical deconvolution (12–15). Also, the model-free methods, known as q-space imaging (16,17), include diffusion spectrum imaging (DSI) (18), and generalized q-sampling imaging (GQI) (19). These methods are widely used to delineate crossing fiber patterns and estimate their tensors in high-angular-resolution DWI data (16–19).

Recently, a novel fast independent component analysis (ICA) tractography method (4) that estimates the orientations of up to three fibers per voxel was proposed to allow the isolation of multiple fibers in clinical DWI data. By assuming that the orientations of all crossing fibers are the same inside each voxel of the local cluster, the ICA method extracts up to three orientations by performing the F-test model selection to estimate an optimal number of crossing fibers in voxels of the cluster. However, the assumption that tracts have a uniform orientation inside the cluster is not necessarily correct in the real brain. Especially at the boundary of different white matter regions where multiple fibers likely cross only at some voxels of the cluster, the sensitivity of the ICA decomposition might be significantly reduced by partial volume effects. In fact, it was found that the ICA method alone does not allow entire delineation of the corticospinal tract (CST) because it fails to track the fibers of those projections in voxels near the precentral gyrus (PCG)/sulcus where fibers of the arcuate fasciculus, the superior longitudinal fasciculus, and the corpus callosum intermingle with the lateral projections of the CST (20).

The present study combines BSM with ICA to further resolve the orientations of multiple fibers within a voxel. The applicability of ICA combined with BSM, termed

[1]Carman and Ann Adams Department of Pediatrics, Children's Hospital of Michigan, Detroit, Michigan, USA.

[2]Department of Neurology, Wayne State University School of Medicine, Children's Hospital of Michigan, Detroit, Michigan, USA.

[3]Translational Imaging Laboratory, Children's Hospital of Michigan, Detroit, Michigan, USA.

[4]Department of Biomedical Engineering, Carnegie Mellon University, Pennsylvania, USA.

[5]Department of Radiology, Wayne State University School of Medicine, Children's Hospital of Michigan, Detroit, Michigan, USA.

Grant sponsor: NIH; Grant number: R01 NS064989.

*Correspondence to: Jeong-Won Jeong, Ph.D., Departments of Pediatrics and Neurology, Wayne State University School of Medicine, Children's Hospital of Michigan, 3901 Beaubien Boulevard, Detroit, MI 48201. E-mail: jeongwon@pet.wayne.edu

Received 21 January 2012; revised 14 August 2012; accepted 15 August 2012.

DOI 10.1002/mrm.24487
Published online 21 September 2012 in Wiley Online Library (wileyonlinelibrary.com).

"ICA+BSM," is demonstrated in computer simulations and clinical DWI data to isolate individual tensors of multiple crossing fibers such as CST, arcuate fasciculus, and superior longitudinal fasciculus fibers at voxels near the PCG and the central sulcus. Based on the hypothesis that multicompartment Gaussian tensors correspond to multiple intersecting fiber bundles present within a voxel, two complementary approaches are combined to isolate multiple fiber bundles within a single voxel: the first is ICA to approximate fiber orientations of multiple tensors existing in a "local cluster," and the second is BSM to refine information across multiple ICA driven tensors mixed into a "single voxel" of a local cluster.

THEORY

The BSM fitting approach (6) is used to supplement the ICA approach to better define fiber bundle orientations within a voxel. For every voxel of white matter, (x,y,z), a small neighborhood cluster of 11 voxels is defined around it by the next nearest voxel, i.e., 3×3 voxels in the x–y-plane, and one voxel above and below the center voxel, (x,y,z), along the z-axis. The diffusion data within this cluster is used to construct the measurement matrix, **U,** whose ith row vector, $\mathbf{u}_i$, represents diffusion sensitizing measurements of all N gradient directions with zero-mean at the ith voxel of the cluster (voxel index $i = 1,2,\ldots,11$); see Eq. 1. Blind source decomposition using a fast fixed point ICA (21) is applied to estimate a generative model that describes how the observed diffusion-weighted signal of $\mathbf{u}_i$ is generated by a process of mixing the statistically independent diffusion processes with zero-mean and unit-variance, $\mathbf{s}_{ij}$ $(j = 1,2,\ldots,11)$ (7).

$$\mathbf{u}_i = \left[\frac{m_{i1}}{m_{i0}} \quad \cdots \quad \frac{m_{iN}}{m_{i0}}\right] - \left[\frac{1}{N}\sum_{n=1}^{N}\frac{m_{in}}{m_{i0}} \quad \cdots \quad \frac{1}{N}\sum_{n=1}^{N}\frac{m_{in}}{m_{i0}}\right] = \sum_{j=1}^{11} a_{ij}\mathbf{s}_{ij} \qquad [1]$$

where m_{in} indicates the signal intensity at the ith voxel of the nth diffusion gradient image, $n = 0$ for the b0 image and $n = 1,\ldots,N$ for the N-diffusion-weighted images. a_{ij} defines a mixing weight for the jth independent component vector, $\mathbf{s}_{ij}$, in the ith voxel measurement that will yield $\mathbf{u}_i$. It is assumed that each of the jth row vectors, $\mathbf{s}_{ij}$ represents either multiple diffusion components independently attenuated per diffusion sensitizing gradient or some unknown confounding artifact. The elements of each row vector, $\mathbf{s}_{ij}$ are latent variables that cannot be directly observed in the elements of the measurements in $\mathbf{u}_i$. The weights of a_{ij} are assumed unknown and are therefore iteratively learned to maximize the statistical independence (or non-gaussianity) between $\mathbf{s}_{ij}$. This configuration involving a neighborhood of 11 voxels allows 11 $\mathbf{s}_{ij}$ vectors to be learned within the framework of an unsupervised neural network (21). In vector–matrix notation, $\mathbf{U} = \mathbf{AS}$ or $\mathbf{S} = \mathbf{A}^{-1}\mathbf{U}$ where the weights of a_{ij} consist of the elements of $\mathbf{A}$. $\mathbf{u}_i$ and $\mathbf{s}_{ij}$ constitute the ith row vectors of $\mathbf{U}$ and $\mathbf{S}$, respectively.

In the present study, principal component analysis (PCA) consisting of a whitening transformation with reduced dimensionality, K, is applied to the measurement matrix, $\mathbf{U}$, to improve the ICA estimation,

$$\tilde{\mathbf{U}} = \left(\mathbf{Y}_K^{-\frac{1}{2}}\mathbf{X}^T\right)\mathbf{U} = \tilde{\mathbf{A}}\hat{\mathbf{S}} \qquad [2]$$

where $\mathbf{X}$ and $\mathbf{Y}$ are the matrices of eigenvectors and eigenvalues in the covariance of $\mathbf{U^T}$, respectively. $\mathbf{Y}$ is a diagonal matrix denoted by $\mathrm{diag}(y_1,\ldots,y_{11})$. $\mathbf{Y}_K^{-1/2}$ represents a diagonal matrix to keep the first K-eigenvalues and disregard other small eigenvalues (i.e., $\mathrm{diag}(y_1^{-1/2}, \ldots, y_K^{-1/2}, 0, \ldots, 0)$), with K representing the assumed number of fiber directions in the measurement, $\mathbf{u}_i$. The superscript T denotes the transpose of a matrix.

Equation 2 reduces the number of sources, $\mathbf{s}_{ij}$, to a scalar K, reduces noise, and prevents overlearning of $\mathbf{s}_{ij}$. It yields a new representation of the diffusion measurement, $\tilde{\mathrm{u}}_i$at the ith voxel,

$$\tilde{\mathbf{u}}_i = \sum_{j=1}^{K}\tilde{\mathrm{a}}_{ij}\mathbf{s}_{ij} \qquad [3]$$

where $\tilde{\mathrm{a}}_{ij}$ denotes the new mixing fraction of the jth source, $\hat{\mathbf{s}}_{ij}$, in $\tilde{\mathbf{u}}_i$ that represents a diffusion profile reconstructed by combining directionally independent K-diffusion processes, $\hat{\mathbf{s}}_{ij}$ without any noise or artifact.

Based on the ICA assumption in Eq. 2, the definition of $\mathbf{u}_i$ in Eq. 1 is substituted into the first term of Eq. 2 whose vector form is eventually equal to Eq. 3. The first line of Eq. 4 shows that this equality results in the new definition of $\tilde{\mathbf{v}}_i$ in the third line of Eq. 4, indicating that $\tilde{\mathbf{v}}_i$ (the diffusion profile with reduced dimension) can be represented as a linear summation of "mean offsets of the diffusion signals reconstructed by whitening and dewhitening" and "uncorrelated-zero-mean-unit-variance diffusion signals of multiple K-fibers" that are directionally independent within voxels of the local cluster. $\tilde{\mathbf{v}}_i$ establishes a formal connection between ICA and BSM, assuming that $\tilde{\mathbf{v}}_i$ approximates a linear summation of the "isotropic diffusion tensor, $\mathbf{D}_{i0}$" and "K-anisotropic tensors, $\{\mathbf{D}_{ij}\}$ of the K-fiber compartments" in the conventional BSM (6,22).

$$\begin{aligned}
&\tilde{\mathbf{U}}_i = \left(\mathbf{Y}_K^{-\frac{1}{2}}\mathbf{X}^T\right)[\mathbf{M} - \overline{\mathbf{M}}], \quad \tilde{\mathbf{V}} = \left(\mathbf{X}\mathbf{Y}_K^{-\frac{1}{2}}\right)\tilde{\mathbf{U}}_i \\
&\tilde{\mathbf{V}} = \left(\mathbf{X}\mathbf{Y}_K^{-\frac{1}{2}}\right)\left(\mathbf{Y}_K^{-\frac{1}{2}}\mathbf{X}^T\right)\mathbf{M} = \left(\mathbf{X}\mathbf{Y}_K^{-\frac{1}{2}}\right)\left(\mathbf{Y}_K^{-\frac{1}{2}}\mathbf{X}^T\right)\overline{\mathbf{M}} + \tilde{\mathbf{A}}\hat{\mathbf{S}} \;= \mathbf{TM} = \mathbf{T}\overline{\mathbf{M}} + \;\tilde{\mathbf{A}}\hat{\mathbf{S}} \\
&\Leftrightarrow \tilde{\mathbf{v}}_i = [\cdots \mathbf{t}_i \cdot \mathbf{m}_n \;\cdots] = [\cdots \mathbf{t}_i \cdot \overline{\mathbf{m}}_n \;\cdots] + \sum_{j=1}^{K}\tilde{\mathrm{a}}_{ij}\hat{\mathbf{s}}_{ij} \\
&\cong \left[\cdots \quad \left(1 - \sum_{j=1}^{K}\mathrm{f}_{ij}\right)\exp(-b\mathbf{r}_n^T\mathbf{D}_{i0}\mathbf{r}_n) \quad \cdots\right] + \left[\cdots \quad \sum_{j=1}^{K}\mathrm{f}_{ij}\exp(-b\mathbf{r}_n^T\mathbf{D}_{i0}\mathbf{r}_n) \quad \cdots\right]
\end{aligned} \qquad [4]$$

where $\mathbf{T}$ represents the product of $\mathbf{X}\mathbf{Y}_K^{-1/2}$ and $\mathbf{Y}_K^{-1/2}\mathbf{X}^T$. $\mathbf{M}$ is a matrix whose ith row and nth column element consists of m_{in}/m_{i0}. $\overline{\mathbf{M}}$ is a matrix whose ith row and nth column element is $\left(\sum_{n=1}^{N} m_{in}/m_{i0}\right)/N$. $\mathbf{t}_i$ indicates the ith row vector of $\mathbf{T}$. $\mathbf{m}_n$ and $\overline{\mathbf{m}}_n$ indicate the nth column vector of $\mathbf{M}$ and $\overline{\mathbf{M}}$, respectively. f_{ij} is the volume fraction of the jth BSM compartment, characterized by the diffusion tensor $\mathbf{D}_{ij}(= \mathbf{E}_j\mathbf{V}_j\mathbf{E}_j^{\mathrm{T}}$, $\mathbf{E}_j$ and $\mathbf{V}_j$ denote eigenvector and eigenvalue matrices, diag(λ_{j1}, λ_{j2}, λ_{j3}), of tensor matrix $\mathbf{D}_{ij}$, respectively). $\mathbf{D}_{i0}$ represents the diffusion tensor of isotropic diffusion. b and $\mathbf{r}_n$ are the b value and the unit vector, respectively, of the N applied diffusion gradients; note: $n = 1,2,\ldots, N$.

The approximation of $\tilde{\mathbf{v}}_i$ using the compartments of BSM can be supported by significant correlations between ICA-driven diffusion components and BSM compartments (Fig. 1). Two cylindrical fiber compartments were generated by BSM (6,22) through parts of Eq. 4, and their ICA components were then estimated by the fast fixed point ICA approach (21) of Eq. 3. It is notable that "mean offsets of the diffusion signals reconstructed by whitening an dewhitening" are highly correlated with the weighted isotropic diffusion profile (Fig. 1a). Weights of individual ICA sources apparently correspond to volume fractions of individual compartments (Fig. 1b). Apparent diffusion coefficients and the first eigenvectors of individual ICA sources are significantly correlated with those of individual compartment signals (Fig. 1c,d). Although ICA is unable to estimate both variance and order of the original sources (21), it is reasonable to assume that ICA-driven diffusion offset and sources can approximate the "isotropic diffusion tensor, $\mathbf{D}_{i0}$" and "K-anisotropic tensors, $\{\mathbf{D}_{ij}\}$ of the K-fiber compartments" in BSM.

The present study parameterizes BSM in Eq. 4 by adopting a single ball and K-stick model (6,22) where all $\mathbf{D}_{ij}$, including $\mathbf{D}_{i0}$, have equal λ_1: the ball compartment of $\mathbf{D}_{i0}$ is completely isotropic ($\lambda_1 = \lambda_2 = \lambda_3$) while the remaining "stick" compartments of all $\mathbf{D}_{ij}$ are perfectly linear ($\lambda_{j1} = \lambda_1$, $\lambda_{j2} = \lambda_{j3} = 0$). For K-fiber terms, this model leads to $K + 1$ compartments and $3 \times K + 1$ degrees of freedom. An optimal number of compartments (or fibers) in $\tilde{\mathbf{v}}_i$, K_{opt} is finally found by the Bayesian Information Criterion (BIC) (23).

$$\mathrm{BIC}_K = \log\left(\frac{\mathrm{RMSE}_K}{N}\right) + \mathrm{p}_K\frac{\log(N)}{N}$$

$$\mathrm{RMSE}_K = \sqrt{\frac{\sum_{n=1}^{N}\left(\tilde{\mathbf{v}}_i^K(n) - \mathbf{v}_i^K(n)\right)^2}{N}}$$

$$\mathbf{v}_i^K = \left[\cdots \quad \left(\sum_{j=1}^{K}\mathrm{f}_{ij}\right)\exp\left(-\mathrm{b}\mathbf{r}_n^T\mathbf{D}_{i0}\mathbf{r}_n\right) + \sum_{j=1}^{K}\mathrm{f}_{ij}\exp\left(-\mathrm{b}\mathbf{r}_n^T\mathbf{D}_{i0}\mathbf{r}_n\right)\right] \quad [5]$$

where p_K is the number of parameters at BSM with K-stick components. RMSE stands for the root mean square error between $\tilde{\mathbf{v}}_i^K$ and $\mathbf{v}_i^K$. A key contribution of ICA+BSM is *not* to use a noisy diffusion measurement of $\mathbf{u}_i$ but to incorporate a diffusion profile, $\tilde{\mathbf{v}}_i$, as a target function for BSM of $\mathbf{v}_i$. As $\tilde{\mathbf{v}}_i$ contains both K-anisotropic ICA components (existing in multiple voxels of the local cluster) and a mean diffusion component (existing only in a center voxel of the local cluster), it represents an explicit diffusion process without any confounding artifacts and directly models the diffusion field existing in a voxel of K-crossing fibers.

In our implementation of Eq. 5, the optimal parameters of f_{ij}, $\mathbf{D}_{i0}$, and $\mathbf{D}_{ij}$ are iteratively refined to minimize the RMSE_K by using the Levenberg–Marquardt fitting algorithm (24) under the following constraints,

$$\sum_{j=1}^{K} f_{ij} = 1, \quad 0.1 \le f_{ij} \le 0.9$$

$$\mathbf{D}_{i0} = \begin{bmatrix}\lambda_1 & 0 & 0\\ 0 & \lambda_1 & 0\\ 0 & 0 & \lambda_1\end{bmatrix} \quad 0.001 \le \lambda_1 \le 0.002$$

$$\mathbf{D}_{ij} = \begin{bmatrix}e_{j1} & 0 & 0\\ e_{j2} & 0 & 0\\ e_{j3} & 0 & 0\end{bmatrix}\begin{bmatrix}\lambda_1 & 0 & 0\\ 0 & 0 & 0\\ 0 & 0 & 0\end{bmatrix}\begin{bmatrix}e_{j1} & 0 & 0\\ e_{j2} & 0 & 0\\ e_{j3} & 0 & 0\end{bmatrix},$$
$$-1 \le e_{j1}, e_{j2}, e_{j3} \le 1 \quad \text{and} \quad \|\mathbf{e}_j\| = 1 \quad [6]$$

where f_{ij} is randomly initialized to have a floating number close to $1/(K + 1)$. λ_1 of $\mathbf{D}_{i0}$ is randomly initialized to have a floating number around 0.0017 mm^2/s. [e_{j1}, e_{j2}, e_{j3}] of $\mathbf{D}_{ij}$ is initialized by the first eigenvector of the diffusion tensor matrix from the ICA source component, $\hat{\mathrm{s}}_{ij}$, in Eq. 3. It is assumed that there exists up to three fiber bundles, $K = 3$, for the BIC selection (i.e., $0 \le K \le 3$). At $K = 0$ (no fiber), only $\{\lambda_{01}\}$ is optimized because there is no ICA component available for [e_{j1}, e_{j2}, e_{j3}] in BSM. For $1 \le K \le 3$, the parameter set of $\{f_{ij}, \lambda_1, e_{j1}, e_{j2}, e_{j3}\}$ is optimized to provide the best fit of $\mathbf{v}_i$ to $\tilde{\mathbf{v}}_i$.

Until a global solution of the Levenberg–Marquardt algorithm is achieved at each K (i.e. $\mathrm{RMSE}_K < 0.01$), the overall fitting process is repeated up to five times with the same ICA driven $\mathbf{e}_j$ but different random values of f_{ij} and λ_1. A minimization of RMSE_K is selected as the global solution of the Levenberg–Marquardt fitting algorithm and then converted into BIC_K of Eq. 5 that includes the cost of penalty caused by the model complexity (i.e., number of parameters). Finally, the index K providing the minimal BIC_K is selected as an optimal number of compartments, K_{opt}. The parameter sets $\{f_{ij}, \lambda_1, e_{j1}, e_{j2}, e_{j3}\}$ providing the global solution at $K = K_{\mathrm{opt}}$ are used to configure K_{opt} stick compartments existing at the ith voxel of the cluster. That is, total K_{opt} fiber orientations are available at each voxel of white matter for the streamline tractography.

METHODS

Subjects and MRI Acquisition

The present study included 20 typically developing children (age: 15.0 ± 3.3 years, 10.1–17.8 years, 10 boys) and two patients with a diagnosis of focal epilepsy. The Human Investigations Committee of Wayne State University granted permission for acquiring MRI scans of all children. All diffusion MRI scans were performed on a 3T GE Signa scanner (GE Healthcare, Milwaukee, WI)

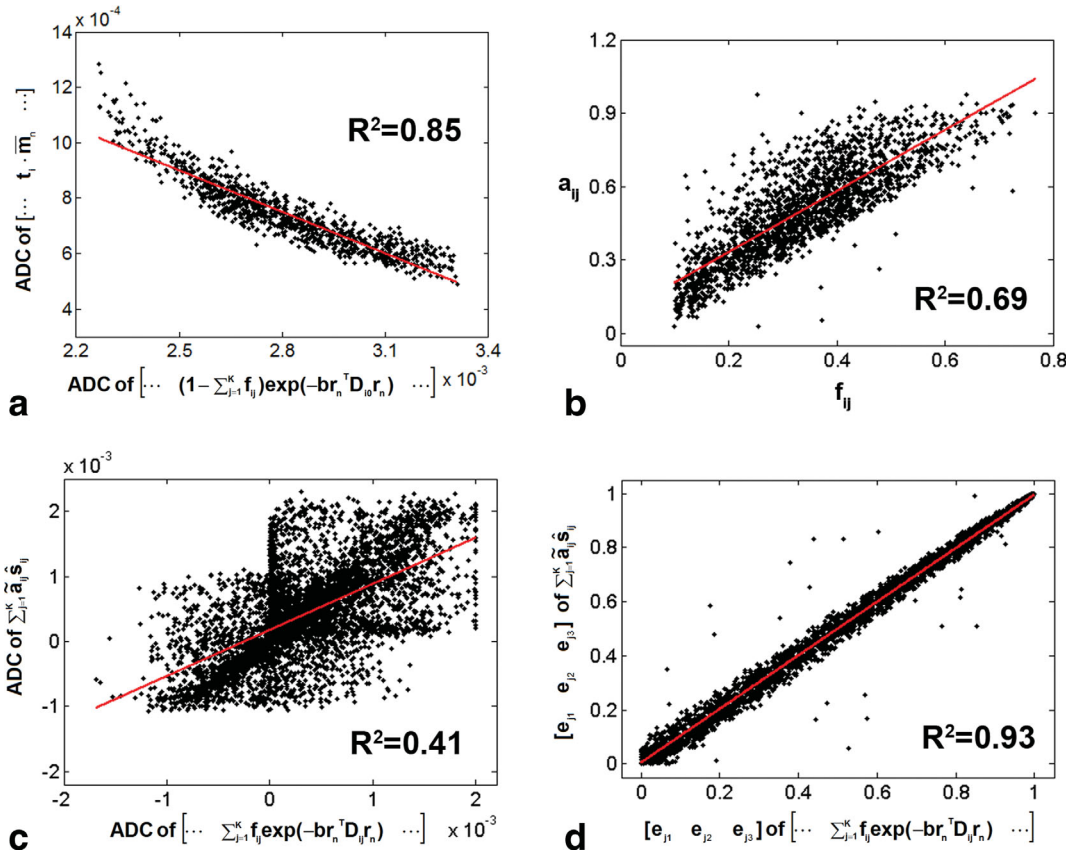

FIG. 1. Correlation between ICA-driven components and BSM compartments. **a**: Apparent diffusion coefficients (ADC) of whitened mean offsets of the diffusion signals versus ADC of the weighted ball compartment. **b**: Weights of individual ICA sources versus volume fractions of individual stick compartments. **c**: ADC of the individual ICA source mixture versus ADC of the individual stick compartment mixture. **d**: The first eigenvectors of individual ICA sources versus the first eigenvectors of individual stick compartments. An isotropic diffusion tensor (D_{i0} with $[\lambda_1,\lambda_2,\lambda_3] = [1.7, 1.7, 1.7] \times 10^{-3}$ mm^2/s) and two-stick tensors ($\mathbf{D}_{ij}$ with $[\lambda_1,\lambda_2,\lambda_3] = [1.7, 0, 0] \times 10^{-3}$ mm^2/s) were randomly mixed using the BSM parts of Eq. 4 with different values of fractions, f_{ij}, and eigenvectors, $[e_{j1}, e_{j2}, e_{j3}]$. For each random mixture of three BSM compartments, ICA-driven components were estimated by the fast ICA approach of Eq. 3. For (a–d), Black dots represent corresponding values of ICA-driven components and BSM compartments to support the experimental feasibility of Eq. 4. The red line indicates the fitted linear regression of the scattered dots. The square of the Pearson correlation coefficient (R^2) was reported to show the correlation between ICA-driven components and BSM compartments. [Color figure can be viewed in the online issue, which is available at wileyonlinelibrary.com.]

equipped with an eight-channel head coil at repetition time (TR) = 12,500 ms, echo time (TE) = 88.7 ms, field of view = 240 cm, 128 × 128 acquisition matrix, contiguous 42 slices with 3 mm thickness using 55 isotropic gradient directions with $b = 1000$ s/mm^2, one $b = 0$ acquisition, and number of excitations = 1.

Computer Simulations

For simulating a single cylindrical compartment, a rank-2 tensor was assumed, $\mathbf{D}_{ij} = \mathbf{E}_j\mathbf{V}_j\mathbf{E}_j^T$ that is completely described by its eigenvector matrix, $\mathbf{E}_j$, and eigenvalue matrix, $\mathbf{V}_j = \mathrm{diag}(\lambda_1,\lambda_2, \lambda_3)$. To simulate $\mathbf{E}_j$, we utilized a random vector with unit norm as the first column vector of $\mathbf{E}_j$ where other elements of $\mathbf{E}_j$ were assumed zeros. Also, to mimic anisotropic diffusion of water molecule at three orthogonal directions, we assumed $\mathbf{V}_j$ of $[\lambda_1,\lambda_2,\lambda_3] = [1.7, 0, 0] \times 10^{-3}$ mm^2/s or $[1.8, 0, 0] \times 10^{-3}$ mm^2/s. An isotropic diffusion compartment, $\mathbf{D}_{i0}$ was simulated with $\mathbf{E}_0 = \mathrm{diag}(1,1,1)$ and $\mathbf{V}_0 = \mathrm{diag}(\lambda_1,\lambda_1,\lambda_1)$. Other anisotropic diffusion compartments, $\mathbf{D}_{ij}$ were simulated by varying $\mathbf{E}_j$ with other random vectors with unit norm and a fixed $\mathbf{V}_j = \mathrm{diag}(\lambda_1,\lambda_2,\lambda_3)$. The crossing angle between two $\mathbf{D}_{ij}$ (called "interfiber angle, α") was ranged from 10° to 80°. For three fibers, the two interfiber angles were assumed to be equal.

The Gaussian mixture model compartments [5] were also used to assess how accurately ICA+BSM can work within a realistic configuration of a multiple fiber mixture. For simulating the mixture of two Gaussian compartments, $\mathbf{D}_{i1}$ and $\mathbf{D}_{i2}$ crossing at different interfiber angles, the eigenvalues of $\mathbf{V}_0$, $\mathbf{V}_1$, and $\mathbf{V}_2$ were changed into $[\lambda_1,\lambda_2,\lambda_3] = [1.7, 1.7, 1.7] \times 10^{-3}$ mm^2/s, $[\lambda_1,\lambda_2,\lambda_3] = [1.7, 0.4, 0.2] \times 10^{-3}$ mm^2/s, and $[1.8, 0.5, 0.3] \times 10^{-3}$ mm^2/s, respectively. $\mathbf{E}_0$ was fixed to diag(1,1,1). A 3 × 3 identity matrix with 1s on the diagonal and 0s elsewhere was randomly rotated in the *x-y-z* plane to generate the eigenvectors of the first fiber, $\mathbf{E}_1$. Discrete interfiber angle (α) was used to parameterize $\mathbf{E}_2$ of the next fiber to rotate $\mathbf{E}_1$ by α in the *x-y-z* plane. Each α was selected randomly to lie within a 10°–80° range and distributed equally within each 10°.

The volume fraction, f_{ij}, were randomly assigned in the range from 0.1 to 0.9 such that $\Sigma f_{ij} = 1$ (i.e., as a

function of K, different ranges of f_{ij} were applied to model the degree of any partial volume effect from an isotropic diffusion compartment, $f_{i0} = 1$ for $K = 0$, $0.1 \leq f_{i1} \leq 0.9$ for $K = 1$, $0.2 \leq f_{i1}, f_{i2} \leq 0.7$ for $K = 2$, $0.2 \leq f_{i1}, f_{i2}, f_{i3} \leq 0.5$ for $K = 3$). A total of 1000 trials per each of the interfiber angles were repeated for each mixture of two and three fibers. For each random trial, multiple fiber compartments were selectively determined in the framework of the BIC model as shown in Eq. 5. The accuracy of recovering fiber orientations was evaluated by the absolute angular error between the actual orientation (first eigenvector of simulated $\mathbf{D}_{ij}$) and the estimated tensor orientation (first eigenvector of recovered $\mathbf{D}_{ij}$).

To assess the effect of heterogeneous voxels on the accuracy of the original ICA method, the percentage of heterogeneous fiber orientations inside the cluster was adjusted in the range 0–0.7 where 0 represents all voxels inside the cluster have crossing fibers with the same orientations (no heterogeneous orientations: "theoretical ICA assumption") and 0.5 represents 50% of voxels have crossing fibers with heterogeneous orientations. Randomly oriented tensors were replaced to simulate the heterogeneous fibers. At each heterogeneous ratio, the errors of ICA+BSM was compared with those of ICA with the F-test model selection (4), "BSM with the random initialization of $\{f_{ij}, \lambda_1, e_{j1}, e_{j2}, e_{j3}\}$ (BSM)" (6,22), "constrained spherical deconvolution (CSD)" (14,15), "BSM with the initialization of $\{e_{j1}, e_{j2}, e_{j3}\}$ using the orientations of local peaks in the orientation distribution function (ODF) obtained from the CSD (CSD+BSM)," DSI (18), and GQI (19). For standalone BSM, a set of $\{f_{ij}, \lambda_1, e_{j1}, e_{j2}, e_{j3}\}$ was randomly initialized as described in Eq. 6. For CSD+BSM, the orientations of local peaks in a CSD-driven ODF were used to initialize $\{e_{j1}, e_{j2}, e_{j3}\}$ of individual stick compartments. Other parameters such as $\{f_{ij}, \lambda_1\}$ were randomly initialized according to Eq. 6. The above scheme of parameter initialization was also applied to human data.

Successful recovery of fiber orientation was assumed if absolute angular error was less than 5°. The rate of this successful recovery was used as another measure for the comparison. The ODF of CSD, DSI, and GQI were obtained using MRtrix package (available at www.nitrc.org) and DSI studio package (available at dsi-studio.labsolver.org) at ODF tessellation = 8 folds and number of peaks = 3. For all trials, Rician noise was randomly added under b0-signal-to-noise ratio (b0-SNR) = 30 to simulate noisy MR diffusion signals.

ICA-Based Ball–Stick Model Tractography

For each voxel of fractional anisotropy (FA) > 0.2, an 11 neighborhood cluster was defined to create a diffusion data matrix, **U**, whose row vectors indicate the diffusion-weighted signals at every voxel of a cluster. The first eigenvectors of K_{opt} tensors resulting from the BIC selection (Eq. 5) were utilized for tractography. The conventional streamline-tracking algorithm was modified to accommodate multiple orientations in voxels (19). At the center of each seeding voxel, tracking was started in the orientation of one fiber that was randomly selected among K_{opt} fibers. The propagation direction was calculated by applying trilinear interpolation on the fiber orientations provided from nearby voxels of the current point. For each nearby voxel, only the fiber orientation that had the smallest turning angle was considered for interpolation.

The lateral projection of CST was used to demonstrate how the ICA+BSM method performs compared with previously reported multifiber solution methods. Fiber orientation maps were generated from all subjects by using six different methods, ICA+BSM, ICA, CSD+BSM, CSD, BSM, and an inhouse implementation of a conventional single diffusion tensor imaging method (DTI, 1,2). The same tractography algorithm was used to propagate streamlines from every voxel in native space. The CST pathway for each subject was sorted from different fiber orientation maps by applying a two-region of interest (ROI) approach, with one seed ROI placed in the PCG and another ROI to select for the fibers in the posterior limb of internal capsule (PLIC). To minimize interoperator variability, binary Montreal Neurological Institute space atlases of both PCG and posterior limb of internal capsule (WFU PickAtlas, www.fmri.wfubmc.edu/software) were placed into native space by applying the inverse of spatial deformation obtained between the subject's b0 image and Montreal Neurological Institute b0 template (25).

To ensure group consistency in tracking the entire CST pathway obtained from each tractography method, a percentage overlap approach was utilized (26). A fiber visitation map was created by counting the number of fibers intersected per voxel (27). The resulting map was normalized to Montreal Neurological Institute space using the spatial deformation derived from the process of normalization of the b0 image, averaged across all subjects, and scaled by a value of maximum visitation in the map, which defines a percentage overlap map. The percentage overlap map of each tractography method was compared with that of a histological atlas of the CST as the gold standard (SPM anatomy toolbox, www.fil.ion.ac.uk). Receiver operating characteristic curve analysis was performed to evaluate the performance of each method.

The ICA+BSM method was further validated by correlating the lateral projections of CST fibers and the primary motor face and hand areas determined by direct brain electrical stimulation in two patients with focal epilepsy. Functional motor mapping using electrical stimulation was performed during extraoperative electrocorticography recordings (28). A site with a contralateral movement induced by stimulation, without after-discharges, was defined as "the primary motor area" for that given body part. Specifically, it was determined whether the CST connecting "hand motor cortex" (seed), posterior limb of internal capsule (first ROI), and "cerebellar peduncles" (second ROI) corresponded to the primary hand CST pathway (29). Then, it was determined whether those connecting "face motor cortex" (seed), posterior limb of internal capsule (first ROI), and "facial colliculus" (second ROI) corresponded to the primary face CST pathway, specially known as the corticobulbar tract (30).

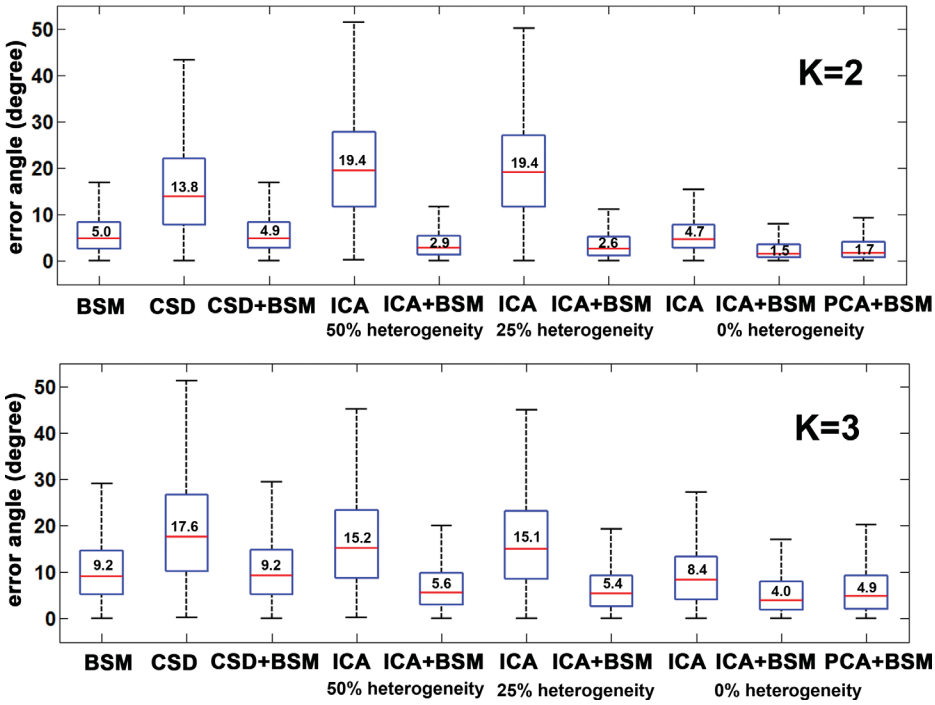

FIG. 2. Error angle between actual and estimated fibers for two and three cylindrical fibers with $[\lambda_1, \lambda_2, \lambda_3] = [1.7, 0, 0] \times 10^{-3}$ mm^2/s. A 55-point shell sampling with *b* value of 1000 s/mm^2 was utilized to generate the simulation data. Each box has lines at the values of the lower quartile (blue colored), median (red colored), and upper quartile (blue colored). The black colored whiskers are lines extending from each end of the quartiles to show the complete extent of the data. **a**: A case of two fibers ($K = 2$). **b**: A case of three fibers ($K = 3$). A b0-SNR = 30 was assumed for (a) and (b). To address how ICA helps BSM to find the global optimum, a diffusion profile reconstructed by PCA including both whitening and dewhitening, $\tilde{\mathbf{v}}_i$ in Eq. 4, was used as a target profile for BSM with five random initializations (PCA+BSM). [Color figure can be viewed in the online issue, which is available at wileyonlinelibrary.com.]

RESULTS

Simulation Studies

Simulation studies assessing the absolute error for two and three fibers per voxel (at the ratio of heterogeneous orientations = 0, 25, and 50%) demonstrated that ICA+BSM is superior to all other methods using BSM, CSD, CSD+BSM, ICA, and PCA+BSM (Fig. 2). The ICA method showed high sensitivity to the ratio of heterogeneous orientations. At 0% (i.e., ICA assumption satisfied), the ICA method showed the smallest error (median value = 4.7°) for two fibers, but errors dramatically increase as the percentage of heterogeneous orientations increases (median value = 19.4°). Meanwhile the percentage of heterogeneous orientations had little effect on absolute errors in ICA+BSM. The ICA+BSM showed the smallest errors (< 2°–7°) in most interfiber angles for two and three fibers. Furthermore, it showed much smaller errors than BSM and CSD+BSM, suggesting that the parametric optimization using the ICA-driven initialization and target diffusion profile provides more accurate solutions in the BSM procedure. Unlike standalone BSM and CSD+BSM that use noisy diffusion measurement, $\mathbf{u}_i$, as a target diffusion profile for BSM optimization, ICA+BSM uses a diffusion profile, $\tilde{\mathbf{v}}_i$, as a target diffusion profile for BSM optimization that represents an explicit diffusion process without any confounding artifacts. The main improvement of ICA+BSM is to minimize error angles at $K = 2$ and 3 resulting from dimensional reduction procedure using PCA, and a small additional improvement is provided by the ICA-based initialization, especially in $K = 3$. This incorporation of $\tilde{\mathbf{v}}_i$ to BSM dramatically reduces errors even in case where ICA alone fails to estimate the

Table 1
Percentage of Trials and Average Number of Updates in Which the Global Solution of Levenberg–Marquardt Curve Fitting Algorithm was achieved by the BIC Model Selection Combined With the Standalone BSM, CSD+BSM, and ICA+BSM

True	No fiber	1	2	3	Updates
Standalone BSM					
No fiber	99.4	0.6	0	0	22
1	0	99.4	0.6	0	30
2	0	0.6	98.8	1.4	62
3	0	18.6	24.0	57.4	128
CSD+BSM					
No fiber	99.4	0.6	0	0	22
1	0	99.6	0.4	0	32
2	0	0.2	98.6	1.2	53
3	0	18.2	21.0	60.8	92
ICA+BSM					
No fiber	99.4	0.6	0	0	22
1	0	99.6	0.4	0	19
2	0	0.2	98.8	1.0	41
3	0	10.8	19.4	71.8	59

For all methods, fractional increment for derivative was set at 10^{-5}. The experimental parameters were iteratively updated until termination tolerance was reached at 10^{-6}.

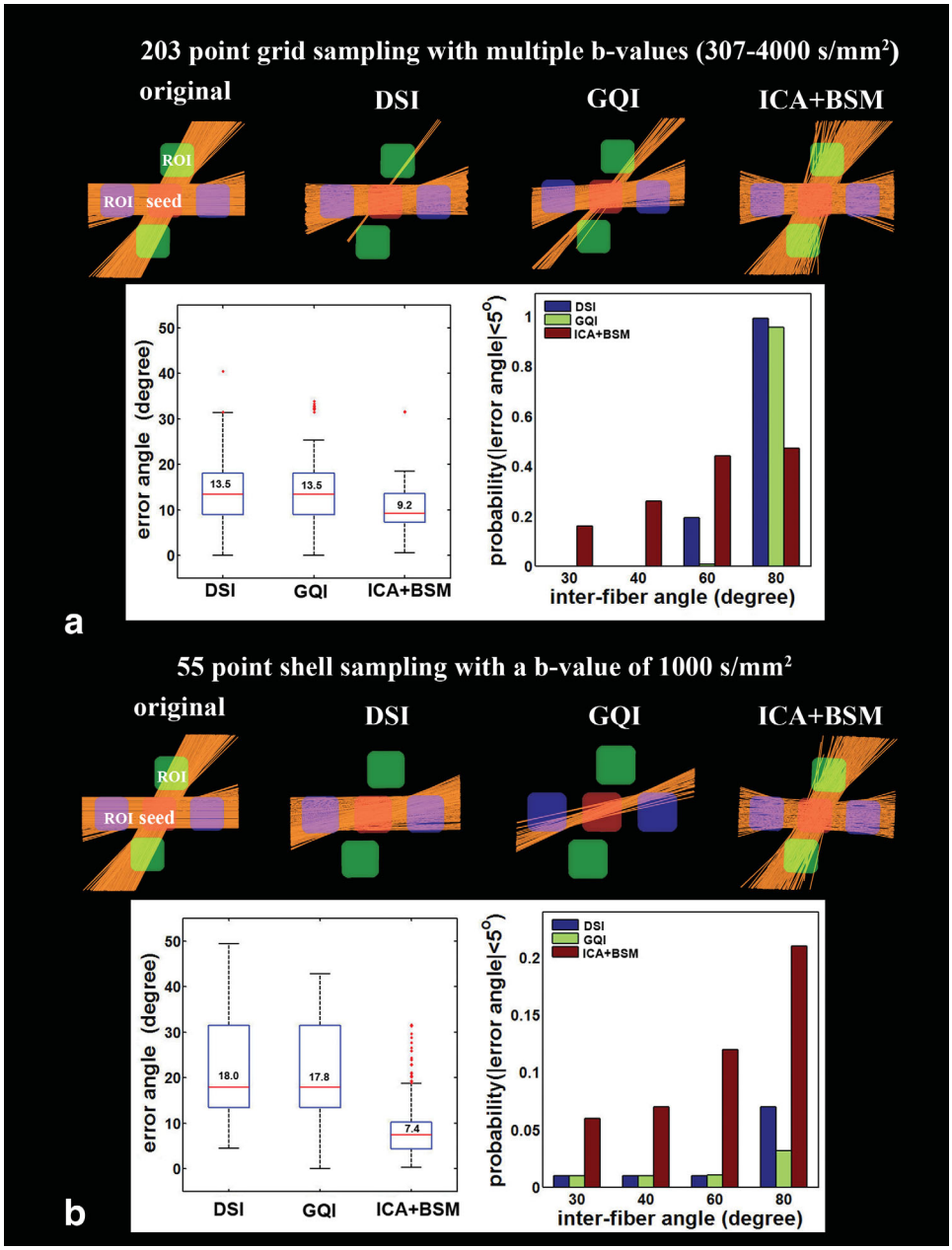

FIG. 3. Error angle between actual and estimated orientation and probability of successful reconstruction for two fibers with different FA values, $[\lambda_1,\lambda_2,\lambda_3] = [1.7, 0.4, 0.2] \times 10^{-3}$ mm^2/s for the first fiber and $[\lambda_1,\lambda_2,\lambda_3] = [1.8, 0.5, 0.3] \times 10^{-3}$ mm^2/s for the second fiber. Blue and green ROIs were used to isolate the tracts of two crossing fibers seeded from red ROI (shown for 60° interfiber angle). Each box of the box plots has lines at the values of the lower quartile (blue colored), median (red colored), and upper quartile (blue colored). The black colored whiskers are lines extending from each end of the quartiles to show the complete extent the data. Red dots represent outliers beyond the ends of the whiskers. **a**: High angular resolution set of 203 grid sampling with multiple *b* values (307–4000 s/mm^2). **b**: Low angular resolution set of 55-point shell sampling with a *b* value of 1000 s/mm^2. A b0-SNR = 30 was assumed for (a) and (b). Note that left boxplot of both panel (a) and (b) reports the result from fiber-crossings of 30°, 40°, 60°, and 80°. [Color figure can be viewed in the online issue, which is available at wileyonlinelibrary.com.]

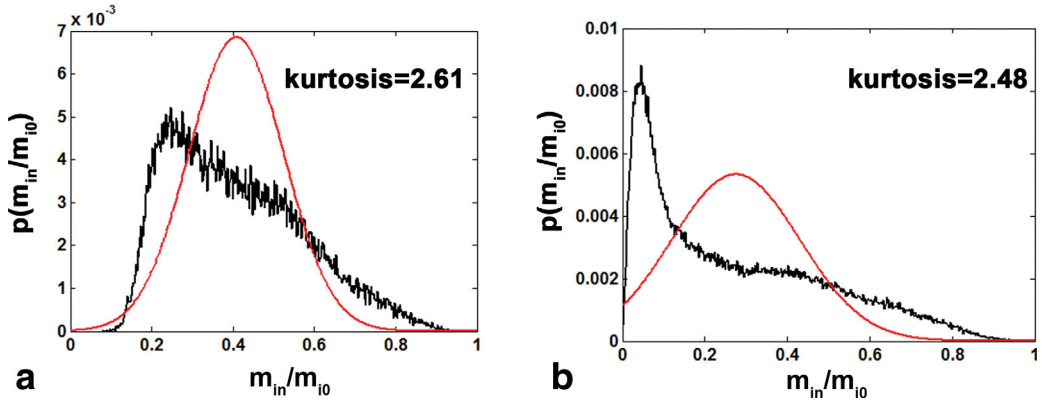

FIG. 4. Examples of the probability density function, $p(m_{in}/m_{i0})$ of the diffusion signals, $u_i = [m_{i1}/m_{i0}, m_{i1}/m_{i0}, \ldots, m_{i55}/m_{i0}]$ generated by BSM (a ball $\mathbf{D}_{i0}$ with $[\lambda_1,\lambda_2,\lambda_3] = [1.7, 1.7, 1.7] \times 10^{-3}$ mm^2/s and a stick $\mathbf{D}_{ij}$ with $[\lambda_1,\lambda_2,\lambda_3] = [1.7, 0, 0] \times 10^{-3}$ mm^2/s) using two different sampling schemes, (**a**) low angular resolution set of 55-point shell sampling with *b* value of 1000 s/mm^2 and (**b**) high angular resolution set of 203 grid sampling with multiple *b* values (307–4000 s/mm^2). A b0-SNR = 30 was assumed for (a) and (b). The $p(m_{in}/m_{i0})$ suggests significant non-Gaussianity of the diffusion signals (i.e., kurtosis > 0). For comparison, a corresponding Gaussian distribution with zero kurtosis is shown in red. [Color figure can be viewed in the online issue, which is available at wileyonlinelibrary.com.]

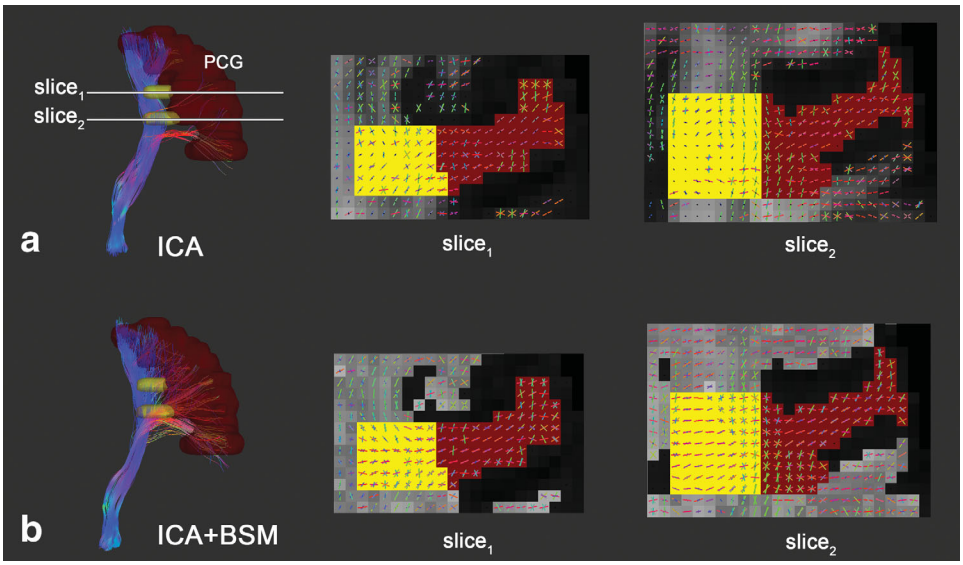

FIG. 5. Independent component analysis tractography combined with a ball–stick model (ICA+BSM) to recover fiber orientations in lateral projections of the corticospinal tract (CST). Brown and yellow clusters indicate the voxels of the precentral gyrus (PCG) and ROIs with crossing fibers, respectively. **a**: Fiber orientations from the ICA method and (**b**) fiber orientations from the ICA+BSM method. The ICA+BSM method could isolate correct orientations of lateral projections (red bars in an ROI of $slice_1$ and $slice_2$) in voxels where the CST intersects with the superior longitudinal fasciculus and arcuate fasciculus. [Color figure can be viewed in the online issue, which is available at wileyonlinelibrary.com.]

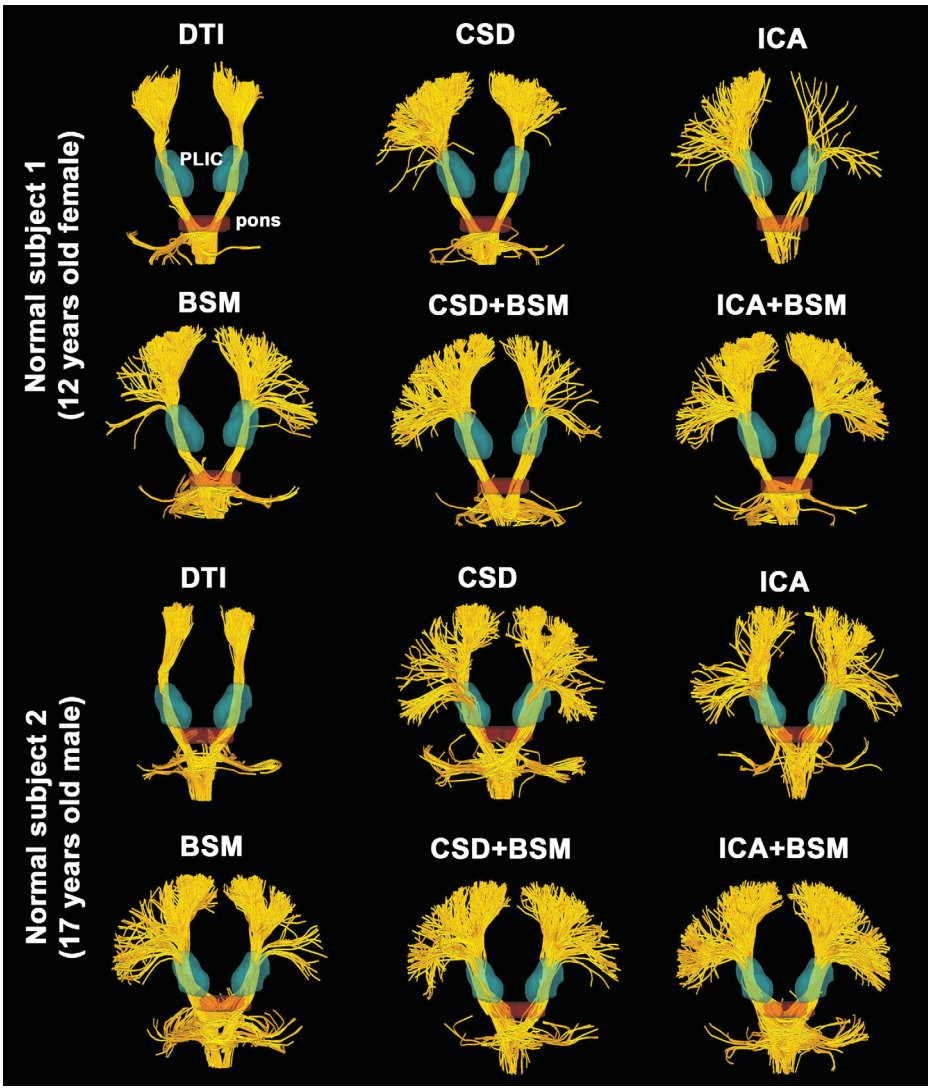

FIG. 6. Comparison of lateral projections of the corticospinal tract obtained from two normal children using single tensor based DTI, CSD, ICA, BSM, CSD+BSM, and ICA+BSM. The same configuration of a seed region (bilateral precentral gyrus: PCG), filtering ROIs (bilateral posterior limb of internal capsule, PLIC: cyan color; pons: red color), and tractography parameters (fraction, $f_{ij} > 0.1$, step size = 20% of voxel width, angular deviation $< 45^{\circ}$, 100 seeds per voxel) was applied for each method. Compared with the other methods, the ICA+BSM imaged more lateral projections connecting the PCG to the pons via the PLIC. [Color figure can be viewed in the online issue, which is available at wileyonlinelibrary.com.]

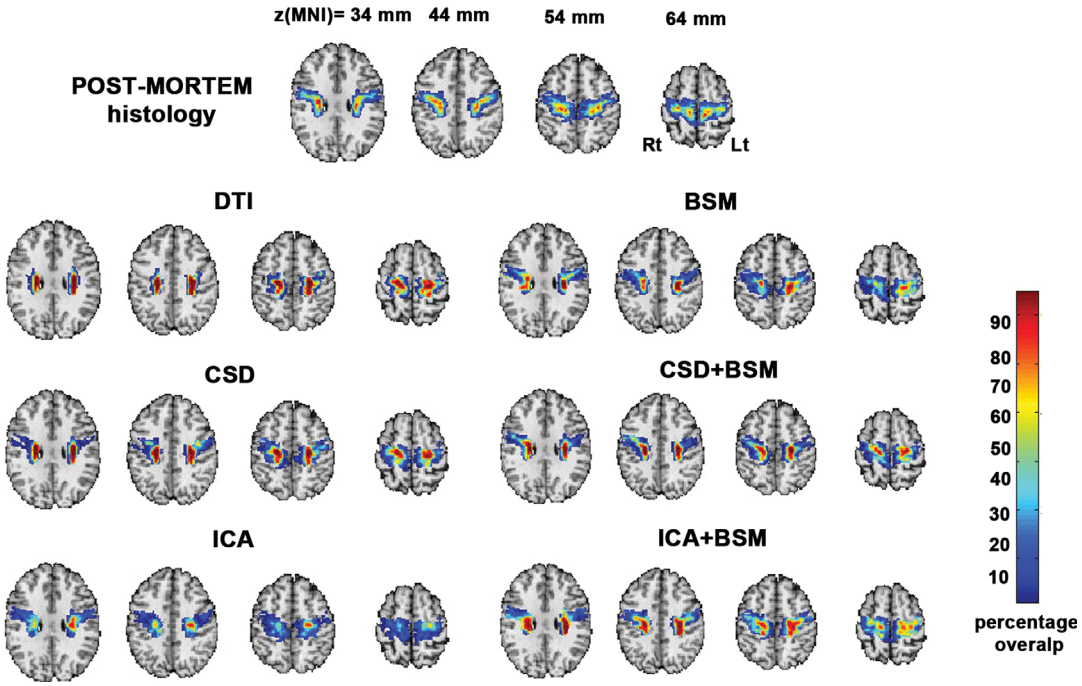

FIG. 7. Comparison between percentage maps of postmortem CST histology and diffusion tractography obtained from single tensor-based DTI, BSM, CSD, CSD+BSM, ICA, and ICA+BSM. The CST tractography of each method was performed from diffusion data of 20 normal controls. The fiber visitation maps of individual subjects were then transformed to Montreal Neurological Institute space by applying the deformation field obtained between the b0 map of individual subjects and the b0 template of Montreal Neurological Institute space. The normalized maps of each method were averaged across subjects and then scaled by the maximum visitation in the map to create a percentage overlap map. The percentage overlap map of each method was finally compared with the postmortem histological map. [Color figure can be viewed in the online issue, which is available at wileyonlinelibrary.com.]

orientations of multiple compartments at high heterogeneity. Also it improves correct BIC selection of the model parameter, K_{opt} at significantly reduced updates by providing the best guesses of experimental parameters to the nonlinear Levenberg–Marquardt curve fitting optimization (Table 1).

The performance of DSI, GQI, and ICA+BSM in resolving two Gaussian tensors with different FA values was also tested with two simulated data sets, ones with high and low angular resolutions, using 203-point grid sampling with multiple b values of 307–4000 s/mm^2 and 55 shell sampling with a b value of 1000 s/mm^2 (Fig. 3). In both angular sampling schemes, the ICA+BSM showed complete reconstructions of two fibers with the smallest errors and also produced the highest probability of successful recovery for most interfiber angles. This result is supported by the fact that high non-Gaussianity of the diffusion signals was properly generated at both angular sampling schemes (Fig. 4), demonstrating that a crucial assumption of ICA+BSM, "diffusion measurement $\mathbf{u}_i$ is a linear mixture of non-Gaussian diffusion components, $\mathbf{s}_{ij}$" was met in simulated data.

Assessment of Clinical Scans

Typical fiber orientations obtained from the voxels of PCG using ICA+BSM are presented in Figure 5. In Figure 5, the CST significantly intersects with arcuate fasciculus and superior longitudinal fasciculus in the two ROIs denoted by yellow boxes in slice$_1$ and slice$_2$. Compared with the ICA, the ICA+BSM images show more lateral components of CST fibers (left to right colored red) in every voxel of each ROI (yellow boxes), suggesting ICA+BSM can successfully identify lateral projections of CST fibers, which the ICA alone fails to realize.

Lateral CST projections were identified by whole brain tractography (Fig. 6) using single tensor-based DTI, CSD, ICA, BSM, CSD+BSM, and ICA+BSM with the same configuration of seed region (bilateral PCG), filtering ROIs (bilateral PLIC and pons), and tractography parameters (fraction, $f_{ij} > 0.1$, step size = 0.2 voxel width, angular deviation $< 45°$, 100 seeds per voxel). The ICA+BSM produced the largest number of lateral projections connecting PLIC to PCG.

To determine whether the additional streamlines identified corresponded to the correct anatomical location of the CST, percentage overlap maps derived from ICA+BSM, ICA, CSD+BSM, CSD, BSM, and DTI were compared with the histological map of the CST atlas (Fig. 7). All methods show a good anatomical correspondence in medial but not lateral portions of the CST. The ICA+BSM achieves substantially larger overlap of lateral CST projections across subjects.

To quantify this larger overlap of the ICA+BSM to identify the histological location of the CST pathway, the receiver operating characteristic curve and accuracy plot were evaluated at five different thresholds of percentage overlap ranging from 2 to 10% (Fig. 8a). The ICA+BSM achieved the highest accuracy at the threshold of 2% where sensitivity/specificity/accuracy = 92.2/

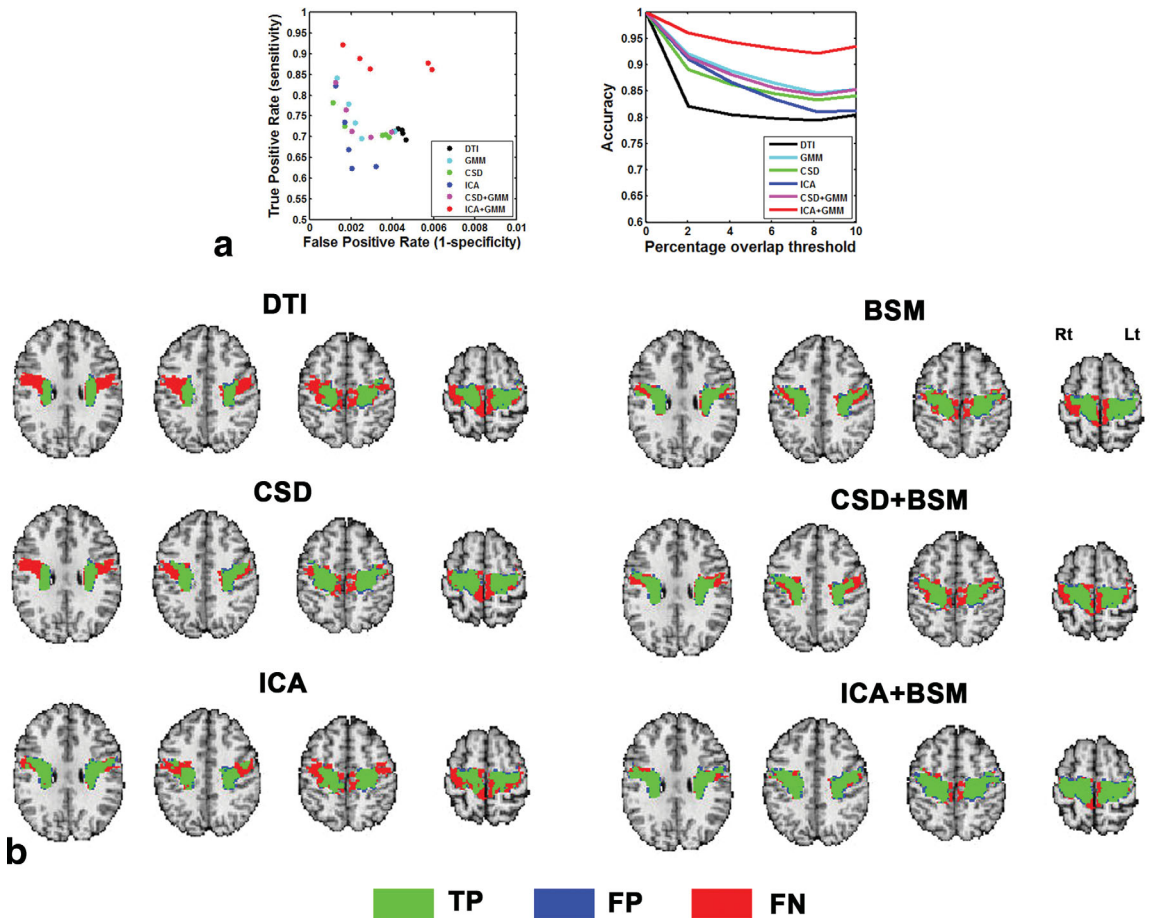

FIG. 8. Assessment of anatomical correspondence achieved by single-tensor based DTI, BSM, CSD, CSD+BSM, ICA, and ICA+BSM tractography. **a**: Receiver operating characteristic curve (left) and accuracy plot (right) were estimated at five different thresholds of percentage overlap, from 2 to 10%. The ICA+BSM achieved the highest accuracy at the threshold of 2% (i.e., sensitivity/specificity/accuracy = 92.2/99.8/96% for ICA+BSM, 82.3/99.9/91.1% for ICA, 78.3/99.9/89.1% for CSD, 84.1/99.9/91.5% for CSD+BSM, 84.3/99.9/92% for BSM, and 71.9/99.5/82.1% for DTI). **b**: For comparison, regions of true positive (TP), false positive (FP), and false negative (FN) at the threshold of 10% were obtained for each method. [Color figure can be viewed in the online issue, which is available at wileyonlinelibrary.com.]

99.8/96% for ICA+BSM, 82.3/99.9/91.1% for ICA, 78.3/99.9/89.1% for CSD, 84.1/99.9/91.5% for CSD+BSM, 84.3/99.9/92% for BSM, and 71.9/99.5/82.1% for DTI. For instance, as presented in Figure 8b showing regions of true positive, false positive, and false negative at the threshold of 10%, the ICA+BSM produced the largest region of true positive (green-colored voxels) and also the smallest region of false negative (red-colored voxels) compared with the other methods.

Validation with the Primary Face and Hand Areas Defined by Electrical Stimulation

The CST fibers of two patients with focal epilepsy were presented in Figure 9. The ICA+BSM method successfully visualized the lateral projections of CST fibers originating from the primary face and hand areas in both patients, where localization of motor pathways is important to minimize the risk of a postoperative motor deficit. Compared with the ICA alone, the ICA+BSM method successfully found the hand CST pathway (red-colored fibers) and face CST pathway (blue-cyan fibers) in both patients.

DISCUSSION AND CONCLUSIONS

Two major findings emerge from this work. First, the parametric optimization of BSM parameters by using ICA-driven eigenvectors, $[e_{j1}, e_{j2}, e_{j3}]$, and target diffusion profile, $\tilde{\mathbf{v}}_i$, dramatically enhances the accuracy of BSM in recovering correct orientations of individual fibers. The simulation study showed that combining ICA with BSM reduces errors up to more than 10° in recovering the orientations of two or three fibers, especially when the interfiber angles are greater than 30°, leading to increased probability of accurate reconstruction up to 5–10%. Second, the ICA+BSM outperforms other voxel-wise BSM methods that parameterize the orientations of multiple fibers using either arbitrary random selection (standalone BSM) or local peaks in ODF (CSD and CSD+BSM). Up to now, most BSM approaches have estimated the likelihood of model parameters based on a raw diffusion profile from an "individual voxel," rather than the diffusion profiles from neighboring voxels that have been utilized for the first time in the present study. In vivo, the crossing of prominent fiber tracts such as arcuate fasciculus and CST is most likely observable in the

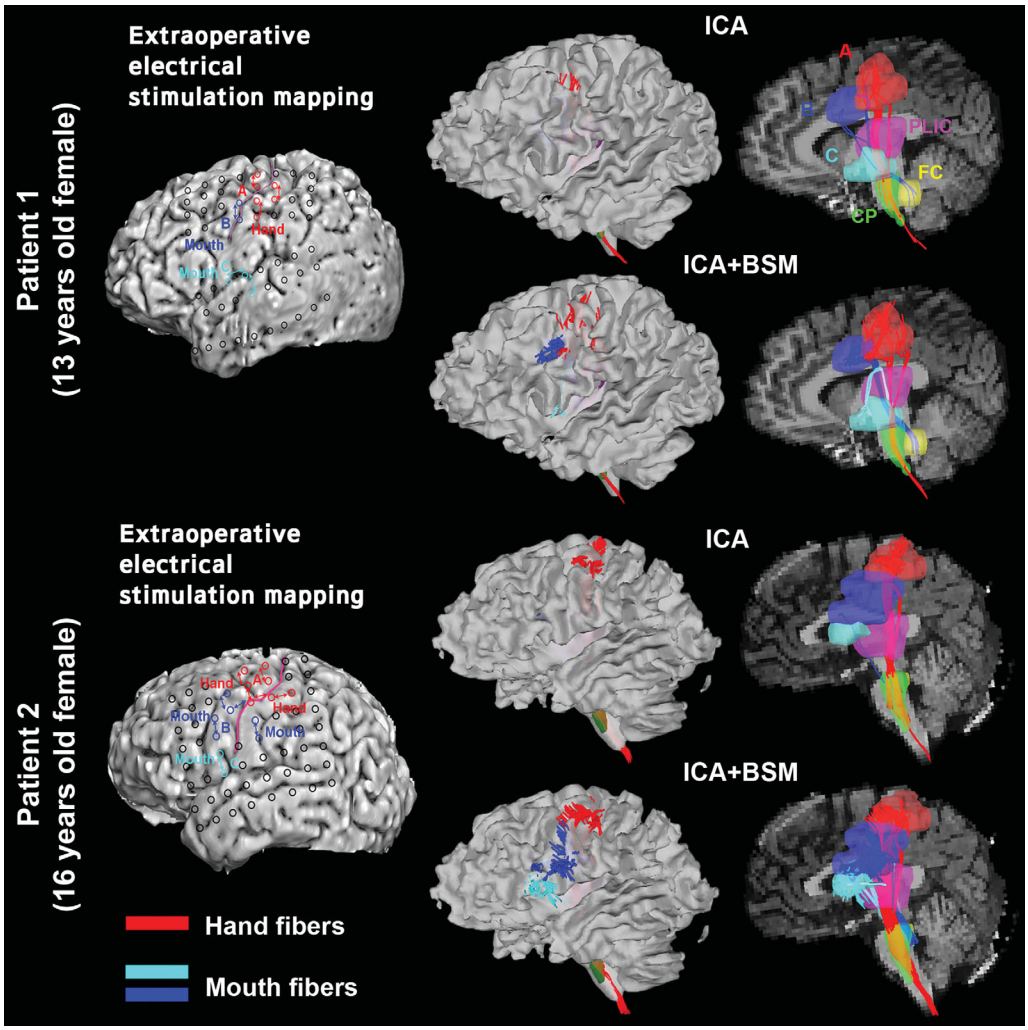

FIG. 9. CST fibers in two patients with focal epilepsy. Extraoperative electrical stimulation determined the primary hand motor areas (A: red) and face motor areas (B: mouth-tongue, blue and C: mouth-lip, cyan). The hand CST fibers connecting the primary hand areas to cerebellar peduncles (CP, green) via the posterior limb of internal capsule (PLIC) were obtained using ICA and ICA+BSM (red fibers). Similarly, the face CST fibers connecting the face motor areas to the facial colliculus (FC) via PLIC were obtained (blue- and cyan fibers). The seed ROIs (motor areas), filtering ROIs (PLIC, CP, and FC), and tractography parameters (fraction, $f_{ij} > 0.1$, step size = 20% of voxel width, angular deviation $< 40^\circ$, 100 seeds per voxel) were identically applied for all cases.

cluster of neighboring voxels. Thus, the independent diffusion processes existing in the cluster can be better estimates of multiple fibers compared with those of multiple fibers observed in a single voxel, that is feasibly suited to be being trapped at local minimum and also require computational complexity in overall fitting procedure. As demonstrated in human studies, the ICA+BSM provided the highest anatomical correspondence to the CST in clinical diffusion data. By successfully imaging the lateral portion of CST, it could increase true positive fibers up to 7–10% whereas it reduced true negative fibers up to 10–15%, compared with the original ICA, BSM, and CSD+BSM methods.

The present study applied dimensionality reduction and ICA to isolate multiple diffusion components that are independently attenuated in each direction of diffusion sensitizing gradients. PCA showed that there exists up to three principal components ($K = 3$) in the covariance of our DWI signals, **U**, accounting for more than 97% of total variance which implies three components are sufficient to explain overall independent diffusion processes. Thus, the diffusion signals at local neighborhood voxels were constructed to a 2D matrix, **U**, sized by voxel (row) $\times$ gradients (column), cleaned by whitening via eigenvalue decomposition with dimensionality, K, and loaded columnwise to estimate an unmixing matrix in the framework of fast ICA. If subsequent model selection such as BIC properly identifies the correct number of components, K_{opt}, mixed in **U**, this configuration will result in K_{opt} MR signal attenuation components that are maximally independent in each of the applied gradient directions. The present study clearly demonstrated that different patterns of these attenuated components feasibly represent independent diffusion processes along multiple axonal fibers crossing at a single voxel.

In the computer simulations, the angular resolution of DSI and GQI was relatively worse than reported in the previous literature, and the discrepancy may be due to

the different diffusion sampling schemes used in the present study. As the diffusion sampling scheme plays an important role in the angular resolution (31), the results of this study may not assert that DSI and GQI cannot resolve fibers at 60° crossing. Although the ICA recovers directionally independent diffusion components with respect to the applied gradient directions, the present study has not fully examined what number of gradient directions and *b* value optimizes the non-Gaussianity of a single fiber to determine the performance of ICA+BSM for clinical DWI study. Future work will thoroughly investigate the effect of the diffusion sampling scheme on the accuracy of ICA+BSM.

For comparison with ICA+BSM, the present study utilized a CSD+BSM that used local ODF peaks as initial estimates of the stick compartments in BSM. As the computer simulations allowed a high volume fraction for an isotropic diffusion compartment to model conservative partial-volume effects from isotropic tissue such as gray matter or cerebrospinal fluid, it might be possible that the standard CSD method used in the present study (14,15) suffers from severe instability due to a high volume fraction of the isotropic diffusion compartment and noise robustness (32), providing subsequent BSM with inaccurate estimation of fiber orientation. The computer simulations of this study supported this possibility by presenting similar accuracy between CSD+BSM and BSM. To overcome this limitation of the standard CSD, a higher-order tensor approximation (22) might be useful. This approximation was designated to incorporate accurate fiber orientations and relative volume fractions that explain the overall ODF. It might be a better alternative to the standard CSD+BSM. The CSD+BSM with the high-order tensor approximation (22) might provide an effective solution to many intravoxel problems in a voxel level, perhaps comparable to the presented ICA+BSM.

In conclusion, the BSM procedure definitely helps to minimize potential errors in voxels where fiber configurations contain incompatible ICA assumptions: (1) multiple fibers are significantly changed in orientation within voxels of a neighborhood cluster, and (2) multiple fibers do not cross all voxels of a neighborhood cluster.

ACKNOWLEDGMENTS

This study was partially funded by a grant from the NIH to E.A.

REFERENCES

1. Basser PJ, Pajevic S, Pierpaoli C, Duda J, Aldroubi A. In vivo fiber tractography using DT-MRI data. Magn Reson Med 2000;44: 625–632.
2. Mori S, van Zijl PC. Fiber tracking: principles and strategies—a technical review. NMR Biomed 2002;15:468–480.
3. McNab JA, Jbabdi S, Deoni SC, Douaud G, Behrens TE, Miller KL. High resolution diffusion-weighted imaging in fixed human brain using diffusion-weighted steady state free precession. Neuroimage 2009;46:775–785.
4. Singh M, Wong CW. Independent component analysis-based multifiber streamline tractography of the human brain. Magn Reson Med 2010;64:1676–1684.
5. Tuch DS, Reese TG, Wiegell MR, Makris N, Belliveau JW, Wedeen VJ. High angular resolution diffusion imaging reveals intravoxel white matter fiber heterogeneity. Magn Reson Med 2002;48: 577–582.
6. Behens T, Woolrich M, Jenkinson M, Johansen-Berg H, Nunes R, Clare S, Matthews P, Bardy J, Simith S. Characterization and propagation of uncertainty in diffusion-weighted MR imaging. Magn Reson Med 2003;50;1077–1088.
7. Hosey T, Williams G, Ansorge R. Inference of multiple fiber orientations in high angular resolution diffusion imaging. Magn Reson Med 2005;54:1480–1489.
8. Peled S, Friman O, Jolesz F, Westin CF. Geometrically constrained two-tensor model for crossing tracts in DWI. Magn Reson Imaging 2006;24:1263–270.
9. Liu C, Bammer R, Acar B, Moseley ME. Characterizing non-Gaussian diffusion by using generalized diffusion tensors. Magn Reson Med 2004;51:924–937.
10. Ozarslan E, Mareci TH. Generalized diffusion tensor imaging and analytical relationships between tensor imaging and high angular resolution diffusion imaging. Magn Reson Med 2003;24: 955–965.
11. Alexander DC, Barker GJ, Arridge SR. Detection and modeling of non-Gaussian apparent diffusion coefficient profiles in human brain data. Magn Reson Med 2002;48:331–340.
12. Kaden E, Knosche TR, Anwander A. Parametric spherical deconvolution: inferring anatomical connectivity using diffusion MR imaging. Neuroimage 2007;37:474–488.
13. Kaden E, Anwander A, Knosche TR. Variational inference of the fiber orientation density using diffusion MR imaging. Neuroimage 2008;42:1366–1380.
14. Tournier JD, Calamante F, Gadian DG, Connelly A. Direct estimation of the fiber orientation density function from diffusion-weighted MRI data using spherical deconvolution. Neuroimage 2004;23: 1176–1185.
15. Tournier JD, Calamante F, Connelly A. Robust determination of the fiber orientation distribution in diffusion MRI: non-negativity constrained super-resolved spherical deconvolution. Neuroimage 2007; 35:1459–1472.
16. Hess CP, Mukherjee P, Han ET, Xu D, Vigneron DB. Q-ball reconstruction of multimodal fiber orientations using the spherical harmonic basis. Magn Reson Med 2006;56:104–117.
17. Descoteaux M, Angelino E, Fitzgibbons S, Deriche R. Regularized, fast, and robust analytical Q-ball imaging. Magn Reson Med 2007;58: 497–510.
18. Wedeen VJ, Wang RP, Schmahmann JD, Benner T, Tseng WY, Dai G, Pandya DN, Hagmann P, D'Arceuil H, de Crespigny AJ. Diffusion spectrum magnetic resonance imaging (DSI) tractography of crossing fibers. Neuroimage 2008;41:1267–1277.
19. Yeh FC, Wedeen VJ, Tseng WY. Generalized q-sampling imaging. IEEE Trans Med Imaging 2010;29:1626–1635.
20. Qazi AA, Radmanesh A, O'Donnell L, Kindlmann G, Peled S, Whalen S, Westin CF, Golby AJ. Resolving crossings in the corticospinal tract by two-tensor streamline tractography: method and clinical assessment using fMRI. Neuroimage 2009;47(Suppl 2): T98-T106.
21. Hyvärinen A, Oja E. A fast fixed-point algorithm for independent component analysis. Neural Comput 1997;9:1483–1492.
22. Schultz T, Westin CF, Kindlmann G. Multi-diffusion-tensor fitting via spherical deconvolution: a unifying framework. Med Image Comput Comput Assist Interv 2010;13(Pt 1):674–681.
23. Feidlin R, Ozarslan E, Komlosh M, Chang LC, Koay C, Jones D, Basser P. Parsimonious model selection for tissue segmentation and classification applications: a study using simulated and experimental DTI data. IEEE Trans Med Imaging 2007;26: 1576–1584.
24. Marquardt DW. An algorithm for least-squared estimation of nonlinear parameters. J Soc Ind Appl Math 1963;11:431–441.
25. Ashburner J. A fast diffeomorphic image registration algorithm. Neuroimage 2007;38:95–113.
26. Ciccarelli O, Toosy AT, Parker GJ, Wheeler-Kingshott CA, Barker GJ, Miller DH, Thompson AJ. Diffusion tractography based group mapping of major white-matter pathways in the human brain. Neuroimage 2003;19:1545–1555.
27. Catani M, Allin MP, Husain M, Pugliese L, Mesulam MM, Murray RM, Jones DK. Symmetries in human brain language pathways correlate with verbal recall. Proc Natl Acad Sci USA 2007;104: 17163–17168.

28. Fukuda M, Nishida M, Juhász C, Muzik O, Sood S, Chugani HT, Asano E. Short-latetency median-nerve somatosensory-evoked potentials and induced gamma-oscillations in humans. Brain 2008;131: 1793–1805.
29. Mettler FA. Extensive unilateral cerebral removals in the primate: physiologic effects and resultant degeneration. J Comp Neurol 1943; 79:185–245.
30. Morota N, Deletis V, Epstein FJ, Kofler M, Abbott R, Lee M, Ruskin K. Brain stem mapping: neurophysiological localization of motor nuclei on the floor of the fourth ventricle. Neurosurgery 1995;37: 922–929.
31. Kuo LW, Chen JH, Wedeen VJ, Tseng WY. Optimization of diffusion spectrum imaging and q-ball imaging on clinical MRI system. Neuroimage 2008 41:7–18.
32. Dell'acqual F, Scifo P, Rizzo G, Catani M, Simmons A, Scotti G, Fazio F. A modified damped Richarson-Lucy algorithm to reduce isotropic background effects in spherical deconvolution. Neuroimage. 2010;19:1446–1458.